Use of infrared thermography to model the effective stress ratio effect on fatigue crack growth in welded T-joints

Lorenzo Bercelli, Bruno Levieil, Cédric Doudard, Benaïssa Malek, Florent Bridier, Anthony Ezanno

Use of infrared thermography to model the effective stress ratio effect on fatigue crack growth in welded T-joints

Lorenzo Bercelli[1*], Bruno Levieil[1], Cédric Doudard[1], Benaïssa Malek[1], Florent Bridier[2], Anthony Ezanno[3]

[1] *ENSTA Bretagne, IRDL - UMR CNRS 6027, 29200 Brest, France*

[2] *Naval Group Research, Technocampus Océan, 5 rue de l'Halbrane, 44340 Bouguenais, France*

[3] *DGA Naval systems center, Avenue de la Tour Royale, BP 40915, 83050 Toulon, France*

Abstract

Welded joints constitute critical components in the high-cycle fatigue dimensioning of naval structures. In particular, the local geometry of the weld toe as well as the welding process induced residual stress strongly impact the fatigue properties. In that regard, such factors must be considered in a dedicated fatigue life forecast model, identified via an adapted experimental protocol. On the basis of X-ray stress analysis and *in-situ* crack growth monitoring by thermoelastic stress analysis, the present study introduces a linear elastic fracture mechanics model that considers the initial residual stress field in the vicinity of the weld toe.

Keywords : stress ratio; fatigue design; linear elastic fracture mechanics; welding; infrared thermography

Nomenclature

$\boldsymbol{E}$	Young modulus	$\boldsymbol{f_m}$	Loading frequency
$\boldsymbol{\nu}$	Poisson coefficient	$\boldsymbol{\sigma_{res}^{init}}$	Local initial residual stress orthogonal to the weld toe
$\boldsymbol{\sigma_y}$	Yield stress	$\boldsymbol{\sigma_{res}^{stab}}$	Local stabilised residual stress orthogonal to the weld toe
$\boldsymbol{\rho}$	Density	$\boldsymbol{\Delta\sigma_{eff}}$	Effective stress range
$\boldsymbol{c}$	Specific heat	$\boldsymbol{R_{eff}}$	Effective stress ratio
$\boldsymbol{\alpha}$	Coefficient of thermal expansion	$\boldsymbol{N}$	Number of cycles
$\boldsymbol{T_0}$	Room temperature	$\boldsymbol{N_{ref}}$	Reference number of cycles (before crack detection)
$\boldsymbol{\vec{q}}$	Local heat flux	$\boldsymbol{N_t}$	Number of cycles to weld long crack
$\boldsymbol{C_{the}}$	Thermoelastic coupling source	$\boldsymbol{N_d}$	Number of cycles to crack detection
$\boldsymbol{\Delta}$	Dissipation source	$\boldsymbol{N_r}$	Number of cycles to sample failure
$\boldsymbol{I_1}$	Stress tensor's first invariant	$\boldsymbol{a}$	Crack surface half-length
$\boldsymbol{I_1}$	Amplitude of the stress tensor's first invariant	$\boldsymbol{c}$	Crack depth
$\boldsymbol{\theta}$	Temperature variation	$\boldsymbol{a_0}$	Deterministic initial crack half-length
$\boldsymbol{\theta_{the}^s}$	Theoretical temperature linked to the thermoelastic coupling	$\boldsymbol{a_f}$	Critical crack half-length
$\boldsymbol{\theta_1^s}$	Theoretical temperature's first harmonic linked to the thermoelastic coupling	$\boldsymbol{k_{sp_1sp_2}}$	Indicator of consistency between crack growth rate and fatigue lifetime of samples
$\boldsymbol{\theta_{the}^c}$	Experimental (infrared camera measurement) temperature linked to the thermoelastic coupling	$\boldsymbol{C_p}$	Paris-Erdogan law constant

[*]*Corresponding author at*: ENSTA Bretagne, IRDL – UMR CNRS 6027, 29200 Brest, France
E-mail address: lorenzo.bercelli@ensta-bretagne.fr

$\boldsymbol{\theta_1^c}$	Experimental (infrared camera measurement) temperature's first harmonic linked to the thermoelastic coupling	$\boldsymbol{m_p}$	Paris-Erdogan law exponent
$\boldsymbol{\Delta\theta_1^c}$	Differential of the temperature's first harmonic linked to the thermoelastic coupling	$\boldsymbol{\Delta K}$	Stress intensity factor range
$\boldsymbol{\Delta\theta_{1_L}}$	Threshold value of the differential temperature's first harmonic linked to the thermoelastic coupling for the detection of cracks	$\boldsymbol{r_o}$	Share of the nominal stress range contribution to crack propagation
$\boldsymbol{\gamma_1}$	Skewness	$\boldsymbol{b}$	Parameter of stress ratio influence
$\boldsymbol{\Delta\sigma_{nom}}$	Nominal stress range	$\boldsymbol{m_R}$	Sensitivity to the effective stress ratio
$\boldsymbol{R_{nom}}$	Nominal load ratio		

1 Introduction

Welded joints constitute a key component to the structural integrity of civilian and military ships. The knowledge of their behaviour in fatigue is critical as they are a common site of crack initiation. In that regard, engineers must be provided with a predictive model dedicated to the fatigue of welded joints. Such model must consider specific factors of influence on fatigue life, namely the geometric singularity of the weld toe and the welding residual stresses which are known to strongly impact the fatigue life of welded-joints [1–4].

The failure mechanism of the welded joint is dependent on the local geometry, and in particular on the curvature radius that marks the transition from the substrate to the weld bead [5,6]. Both the welding process (number of welding passes, power input, …) and post-welding operations (grinding, remelting, shot peening, …) can significantly affect this local geometry, thus the high cycle fatigue properties [7]. For instance it was shown by Carteron *et al.* [8], on Gas Metal Arc Welding cruciform welded joints, that TIG remelting could further delay the initiation of cracks, changing from a crack propagation dominated (in the as-welded condition) to a crack initiation dominated fatigue life.

The welding residual stress field is also strongly dependent on the welding and post-welding process parameters [9–11]. Moreover, it can be altered by the in-service cyclic loading [12], especially at the weld toe where plasticity can occur. The resulting stabilized residual stress field affects the high cycle fatigue life of the welded joint as it adds up with the mean stress, locally altering the stress ratio. In that regard, Hensel proposed the introduction of an effective stress ratio R_{eff}, taking into account the stabilized residual stress, and defined a mean stress sensitivity factor m_R, that links the stress range $\Delta\sigma(R_{eff}, N)$ for any stress ratio R_{eff} to the reference stress range $\Delta\sigma(R_{eff} = -1, N)$ for a constant fatigue life N [13]. The parameter m_R is found to be dependent both on the material and welded joint configuration. Other approaches rely on Linear Elastic Fracture Mechanics (LEFM), via the introduction of the stress ratio R in the Paris-Erdogan law [14] in order to directly model the fatigue crack growth [15–17]. Indeed, as it is demonstrated in the work by Smith and Smith [18], while the local residual stresses near the weld toe have little effect on the crack initiation phase, it significantly affects the crack growth rate.

In such context, the knowledge of the failure mechanism as well as the accurate stress state in the vicinity of the weld toe is crucial to forecast the fatigue life of a welded joint. In this study, thick high strength steel T welded-joints are considered. The assessment of the residual stresses at the weld toe is done through X-ray diffraction. To explore the mean stress effect on fatigue life, Thermoelastic Stress Analysis (TSA) is chosen. Indeed, TSA has proven to be especially suited to the monitoring of surface cracks [19,20], and has already been used successfully in the case of cruciform welded-joints [8,21]. A dedicated post-processing method of the collected infrared data allows for the assessment of fatigue crack growth properties useful to the identification of a LEFM based model.

This paper is divided in three sections. Firstly, details are given about the welded-joint configurations studied in fatigue and the associated experimental set-up. The specific protocols of residual stress assessment through X-ray diffraction as well as fatigue cracks monitoring using TSA are also presented. Secondly, experimental results are detailed, both on the fatigue performance of each tested joint and the post-processing of infrared data; the failure mechanism is determined on the basis of TSA observations. Thirdly, a fatigue model is presented, based on a LEFM approach: the influence of the effective stress ratio R_{eff} is considered in the Paris-Erdogan law through a sensitivity parameter b^*. The parameters of the proposed model are determined on the basis of the crack propagation kinetics identified by TSA. It is found that the mean stress sensitivity m_R relative to this model is coherent with the findings of Hensel [13] and that the fatigue life forecasts for different load ratios are in good agreement with experimental results.

2 Experimental set-up and methods

In this section, are presented the test protocol, the studied specimen and the experimental methods, namely residual stress measurement through X-ray diffraction and fatigue cracks monitoring through TSA.

2.1 Test set-up and equipment

Tests were performed on thick welded T-joints made of ferritic high-strength steel ($R_{p_{0.2}} \geq 700\ MPa$, $R_m \geq 780\ MPa$ and $A_{\%} \geq 15\ \%$) used for naval applications. Dimensions of the T-joints are detailed in Figure 1 (thickness e_T is not given for confidentiality purposes).

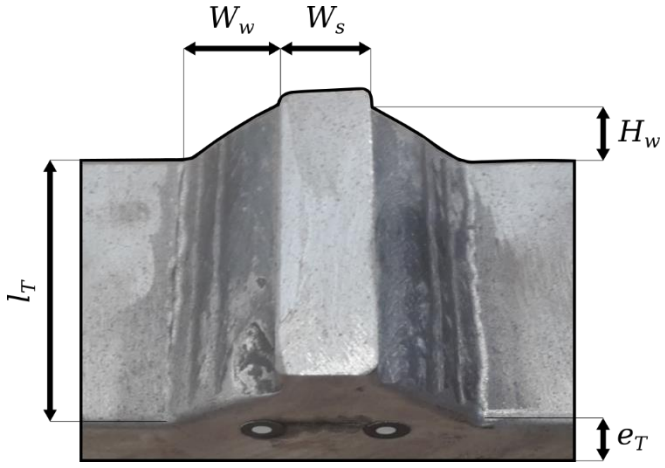

$\boldsymbol{l_T}$	49
$\boldsymbol{W_s}$	14
$\boldsymbol{W_w}$	15
$\boldsymbol{H_w}$	15

Figure 1: Welded T-joint dimensions (in millimetres)

Tests were carried out using a four-point bending fixture mounted in a hydraulic tensile machine of a $100\ kN$ load capacity. The testing machine is load controlled in order to apply a sinusoidal cyclic loading. The T-joints are monitored during the test by recording infrared films at a regular time interval. The infrared camera sampling frequency is $100\ Hz$ and films were consistently 3000 frames long. Given the the presence of the four-point bending fixture, an infrared mirror of reflectivity of 98 % tilted at 45° was used, thus allowing for the infrared monitoring of both the weld toes and the side of the T-joint (Figure 2).

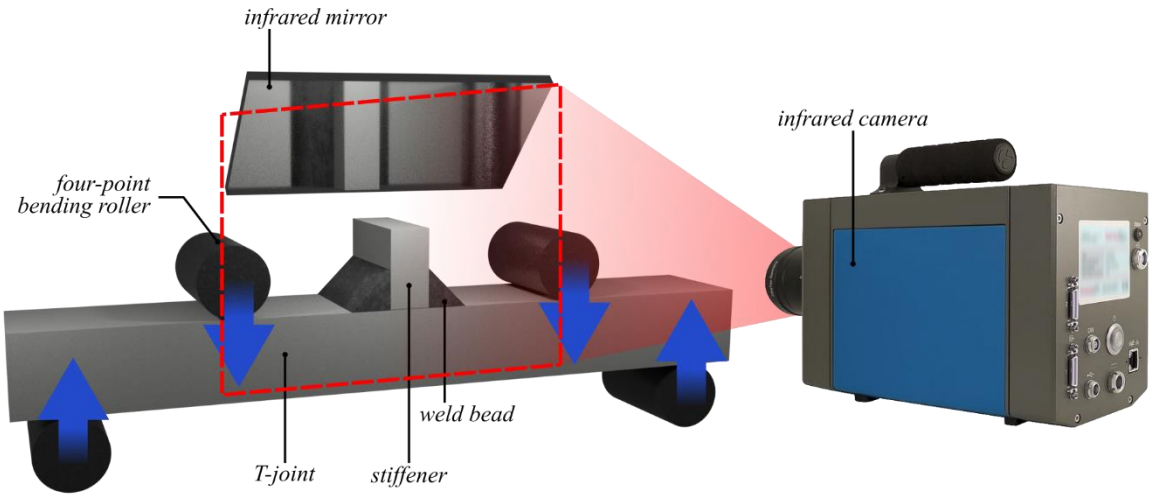

Figure 2: Illustration of the four-point bending test set-up configured for the loading ratio $R_{nom} = 10$

In order to explore the coupled effect of the load stress ratio and the residual stresses in the vicinity of the weld toe on the fatigue life of the welded joints, four testing configurations were considered in this study:

- AS-W-R01: in the as-welded state and tested at the load ratio $R_{nom} = 0.1$;
- AS-W-R10: in the as-welded state and tested at $R_{nom} = 10$;
- PRE-T-R01: pre-loaded in tension at a nominal stress σ_y and tested at $R_{nom} = 0.1$;
- PRE-C-R10: pre-loaded in compression at a nominal stress $-\sigma_y$ and tested at $R_{nom} = 10$.

A pre-loading in tension of the welded T-joint tends to introduce negative (compression) residual stresses normal to the weld toe, while a pre-loading in compression tends to introduce positive (tension) residual stresses normal to the weld toe.

2.2 Residual stresses at the weld toe

Residual stresses were measured using a StressTech G2R X-ray diffractometer and the $sin^2\psi$ method. Surface measurements were made with a 1 mm collimator to measure as closed as possible to the weld toe. Several measurements were made to obtain an average value as the residual stress vary at the weld toe along the welding direction. Only the transverse stress (perpendicular to the weld toe) is reported in this paper as it is aligned with the maximum principal stress during fatigue.

Residual stresses were measured after welding and after the introduction of the loading prior to fatigue testing to obtain the initial residual stress. Specimens were measured again during the fatigue test to obtain a stabilised residual stress value, which is used as the reference value in the present proposed predictive model. Indeed, it is observed that residual stresses stabilise already after a few loading cycles, before any fatigue crack detection by Thermoelastic Stress Analysis (TSA). Measured residual stresses are detailed in Table 1.

Sample	**Initial state**	R_{nom} $(-)$	$\frac{\Delta\sigma_{nom}}{\sigma_y}$ $(-)$	$\frac{\sigma_{res}^{init}}{\sigma_y}$ $(-)$	$\frac{\sigma_{res}^{stab}}{\sigma_y}$ $(-)$	R_{eff} $(-)$
AS-W-R01-1	AS-W	0.1	0.29	-0.07	-0.07	-0.2
AS-W-R01-2	AS-W	0.1	0.66	-0.07	-0.07	0
AS-W-R01-3	AS-W	0.1	0.86	-0.07	-0.21	-0.2
PRE-T-R01-1	PRE-T	0.1	0.66	-0.21	-0.21	-0.3
AS-W-R10-1	AS-W	10	0.66	-0.07	-0.07	5.5

Sample	Initial state	R_{nom} (−)	$\frac{\Delta\sigma_{nom}}{\sigma_y}$ (−)	$\frac{\sigma_{res}^{init}}{\sigma_y}$ (−)	$\frac{\sigma_{res}^{stab}}{\sigma_y}$ (−)	R_{eff} (−)
AS-W-R10-2	AS-W	10	1.13	-0.07	0.43	-3.9
PRE-C-R10-1	PRE-C	10	0.66	0.14	0.14	-8.4
PRE-C-R10-2	PRE-C	10	0.86	0.14	0.14	-17
PRE-C-R10-3	PRE-C	10	1.13	0.14	0.43	-3.9

Table 1: Detail of the initial state, loading configuration, initial and stabilised residual stress and effective stress ratio of each tested sample

The presence of a residual stress field in the vicinity of the weld toe must be considered as it affects the local stress state responsible for the initiation and propagation of fatigue cracks. For this purpose, the effective stress ratio R_{eff} (*i.e.* a stress ratio at the vicinity of the weld toe) is defined as

$$R_{eff} = \frac{\sigma_{min} + \sigma_{res}^{stab}}{\sigma_{max} + \sigma_{res}^{stab}} \quad (1)$$

where σ_{res} is the component of the residual stress tensor in the direction of the principal maximum nominal stress and where σ_{min} and σ_{max} are the minimal and maximal nominal stress in a cycle, respectively. This definition of the effective stress ratio is inspired by the work of Hensel [13].

The values of this effective stress ratio for all tested T-joints are detailed in Table 1. As it can be observed, the presence of residual stresses can strongly impact the effective stress ratio in the vicinity of the weld toe, especially for pre-loaded configurations. It is important to note that while only two nominal stress ratios R_{nom} are tested, there are in fact seven different effective stress ratios R_{eff} due to the presence of residual stresses at the weld toe.

2.3 Infrared thermography for the detection of cracks

Thermography has proven to be an effective and versatile experimental method for the characterization of the fatigue behaviour of welded joints. For instance it allows for the characterization of a local heat dissipation behaviour useful to the assessment of a predictive fatigue model [8,22,23]. It can also be used for a rapid assessment of the fatigue strength [24–26], based on an empiric self-heating approach [27]. In another approach, Williams *et al.* [28] demonstrated the applicability on welded materials of the thermographic method for the determination of the remaining fatigue life, as proposed by Amiri *et al.* [29]. Finally, thermography, or more specifically TSA, can be used for the detection and the monitoring of fatigue cracks at the weld toe and the assessment of a fatigue crack growth rate [8,21]. In this study, fatigue crack monitoring via TSA was the selected approach.

2.3.1 Theoretical background

This method relies on the analysis of the temperature response θ of a structure submitted to a cyclic loading. Such dissipative behaviour can be decomposed in two contributions, namely:

- the intrinsic dissipation, responsible for a progressive temperature rise towards a stabilized temperature θ_d (assuming the heat source averaged over one loading cycle is constant);
- the thermoelastic coupling, responsible for the immediate thermal response θ_{the}^{S} of a loaded structure.

In this study, the temperature linked to the thermoelastic coupling is of particular interest as it allows for mechanical field measurement on the observed surface. Indeed, the local heat equation is written

$$\rho c \frac{\partial \theta}{\partial t} = -div(\vec{q}) + C_{the} + \Delta, \quad (2)$$

where ρ is the density, c the specific heat, θ the temperature variation, $\vec{q}$ the local heat flux and C_{the} and Δ the heat sources of thermoelastic coupling and dissipation, respectively. For small temperature

variations θ (i.e. $\frac{\theta}{T_0} \ll 1$ where T_0 is the initial temperature), the thermoelastic coupling heat source C_{the} can be written [30]

$$C_{the} = -T_0\alpha\left(\dot{I}_1 + \alpha\dot{\theta}\frac{3E}{1-2\nu}\right), \quad 3$$

where α is the coefficient of thermal expansion, I_1 is the stress tensor's first invariant, E is the Young modulus and ν is the Poisson coefficient. Noting that, for typical steel materials at room temperature $\alpha^2\frac{3E}{1-2\nu}T_0 \ll \rho c$, and solving the local heat equation for an isotropic material under adiabatic conditions, it comes

$$\frac{\partial\theta_{the}^S}{\partial t} = \frac{-T_0\alpha}{\rho c}\frac{\partial I_1}{\partial t}, \quad 4$$

with θ_{the}^S the temperature variation linked to the thermoelastic coupling. For a linear system (undamaged purely elastic structure), given a sinusoidal macroscopic loading of frequency f_m, equation 3 links the temperature to the thermoelastic coupling θ_{the}^S, which is also sinusoidal at the frequency f_m, and its amplitude (the first harmonic) is written

$$\theta_1^S = I_{1_a}\frac{\alpha T_0}{\rho c}, \quad 5$$

with I_{1_a} the amplitude of the stress tensor's first invariant.

In practice, the temperature at the surface of a structure is recorded over a few loading cycles using an infrared camera. This experimental temperature signal includes both the conduction effects and the surface emissivity. The field of the first harmonic of the temperature signal linked to the thermoelastic coupling θ_1^c is estimated from infrared data by the lock-in method [31–33], as the loading frequency f_m is known. This field is an image of the mechanical field I_{1_a}, locally averaged because of conduction effects; indeed, the testing conditions are not adiabatic ($f_m < 5\ Hz$). Nevertheless, stress heterogeneities at the surface of the T-joint can be observed, as illustrated in Figure 3. Inside a same field of view, a classical bending stress field is revealed on the side of the joint, and stress concentrations at the weld toes around the stiffener are visible in the infrared mirror frame.

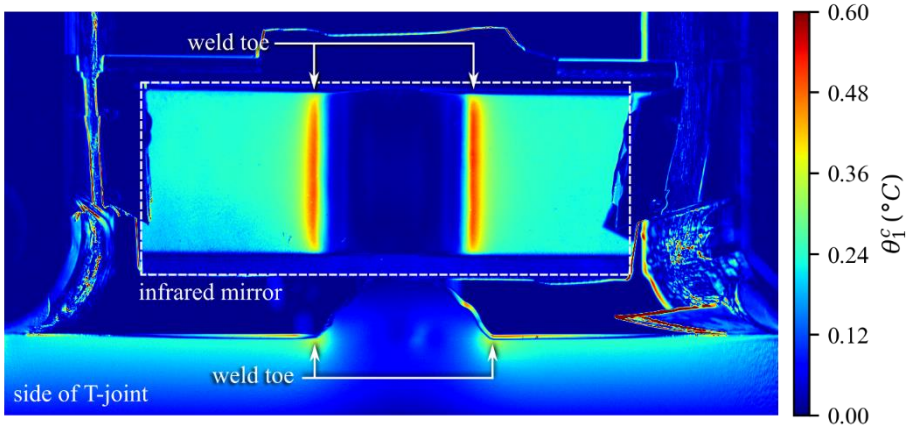

Figure 3: Field of the temperature's first harmonic θ_1^c linked to the thermoelastic coupling on a T-joint determined by the lock-in method from an infrared film

When the structure is damaged, in particular when fatigue cracks have initiated, the mechanical field is affected. As a result, surface cracks can be revealed in the infrared data. In the case of the bending of T-joints, surface cracks initiate at the weld toe, and propagate in Mode I. To reveal such cracks in the infrared images, two cases must be distinguished according to the considered loading ratio.

2.3.2 Crack detection at $R_{nom} = 0.1$

At $R_{nom} = 0.1$, fatigue cracks are always open. The system is linear, *i.e.* given a sinusoidal macroscopic loading the local temperature linked to the thermoelastic coupling θ^{S}_{the} around the crack is sinusoidal. The crack lips being free edges, the local amplitude of the stress tensor's drops drastically. As a result, the presence of an opened crack at the weld toe of a T-joint is easily detectable as it is responsible for a distinct discontinuation of the linear concentration of θ^{c}_{1} along the weld toe (Figure 4 a), as determined by the lock-in method [31]. In practice, in order to detect the presence of a fatigue crack as early as possible, differential maps of the temperature's first harmonic linked to the thermoelastic coupling θ^{c}_{1} are calculated considering a reference state where no cracks exist

$$\Delta\theta^{c}_{1}(N) = \theta^{c}_{1}(N) - \theta^{c}_{1}(N_{ref}), \qquad 6$$

where $\Delta\theta^{c}_{1}$ is the differential of the temperature's first harmonic, N is the considered number of cycles and N_{ref} is the number of cycles of the reference state (Figure 4 b). In this study, a threshold value of $\Delta\theta_{1_L} = 0{,}03°C$ is chosen to detect open cracks at the weld toe when considering a loading ratio of $R_{nom} = 0.1$.

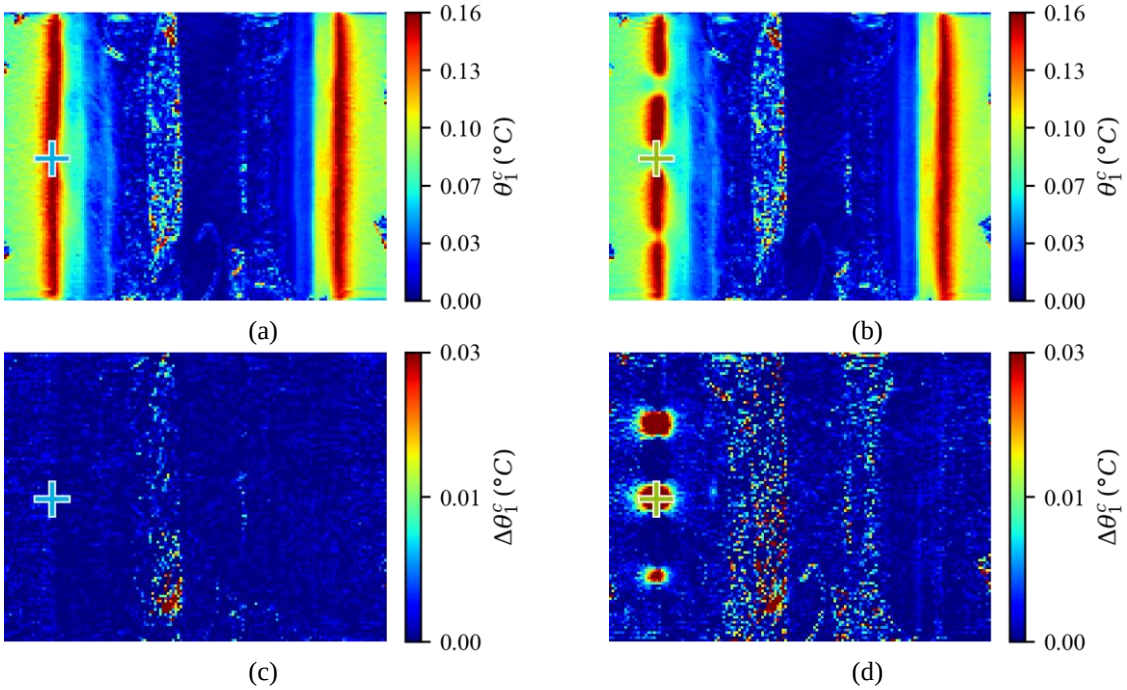

Figure 4: Image post-processing example on a damaged sample under cyclic bending at $R_{nom} = 0.1$ - Field of the temperature's first harmonic θ^{c}_{1} at $N = 62\,000$ cycles (a) and at $N = 160\,000$ cycles for which three cracks on the left weld toe are visible (b) and corresponding fields of the differential of the temperature's first harmonic $\Delta\theta^{c}_{1}$ at $N = 62\,000$ cycles (c) and at $N = 160\,000$ cycles (d) – The temperature signals θ^{c}_{the} at the coloured cross markers are illustrated in Figure 5 a

2.3.3 Crack detection at $R_{nom} = 10$

At $R_{nom} = 10$, because of the high compressive local mean stress at the weld toe, fatigue cracks are subject to a closing phenomenon. The crack lips constitute free edges for only a portion of a loading cycle; the crack is closed for the rest of the time, transmitting a compressive load. As a result, the system is no longer linear: the application of a sinusoidal macroscopic loading does not result in a sinusoidal local temperature signal. Rather, given the intermittent closing phenomenon, the local temperature signal θ^{S}_{the} is similar to a clipped sine. This is illustrated in Figure 5 a, in which the temperature signal θ^{c}_{the} over time in one pixel at the weld toe (exact positions are illustrated in Figure 4 and Figure 6), before and after crack initiation at both $R_{nom} = 0.1$ and $R_{nom} = 10$. For such signals, the first harmonic θ^{c}_{1} is no longer a suitable indicator and the lock-in method cannot be used to detect closing fatigue cracks

efficiently. Instead, another method is proposed, through the analysis of the distribution of the temperature signal T^c values sampled over an integer number of periods. This distribution is symmetrical with respect to the mean value when T^c is a sine signal (as for the tests at $R_{nom} = 0.1$ for which no crack closing occur) and it is no longer symmetrical when T^c is a clipped sine (as for the tests at $R_{nom} = 10$ for which crack closing occur) as it is illustrated in Figure 5 b. To measure the asymmetry of the distribution of a random variable X, one can use the skewness indicator γ_1, defined as

$$\gamma_1(X) = \mathbb{E}\left[\left(\frac{X-\mu}{\sqrt{v}}\right)^3\right], \qquad 7$$

Where $\mathbb{E}$ is the expectancy, μ is the mean of the random variable X and v is its variance. The skewness is zero for a perfectly symmetrical distribution, and non-zero otherwise. As such, maps of the skewness γ_1 are calculated from the infrared films. In this study, a threshold value of $\gamma_{1_L} \approx 0.05$ is chosen to detect closing cracks at the weld toe when considering a loading ratio of $R = 10$. One should note that the threshold values $\Delta\theta_L$ are γ_{1_L} not directly comparable in terms of crack size as the two detection methods do not rely on the same quantity. Their values were chosen as small as possible in order to avoid seeing measurement noise as fatigue cracks.

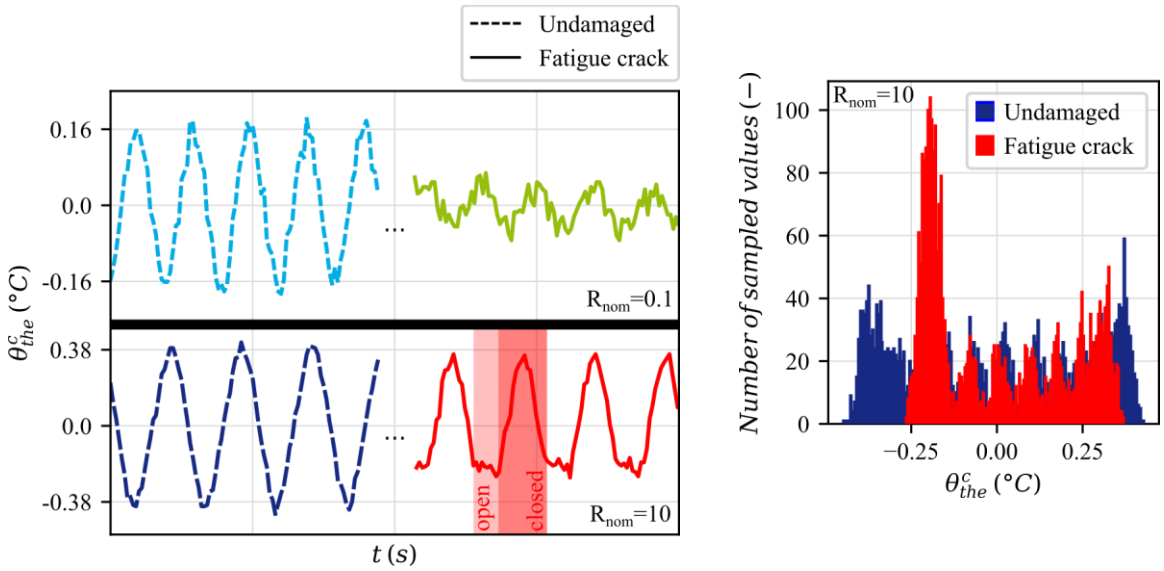

(a) (b)

Figure 5: Temperature linked to the thermoelastic coupling θ^c_{the} at the weld toe over time t as determined by the infrared camera for loadings at $R_{nom} = 0.1$ and $R_{nom} = 10$, both for undamaged and cracked state (a) and sampled signals' distributions at $R_{nom} = 10$ for undamaged and cracked state (b)

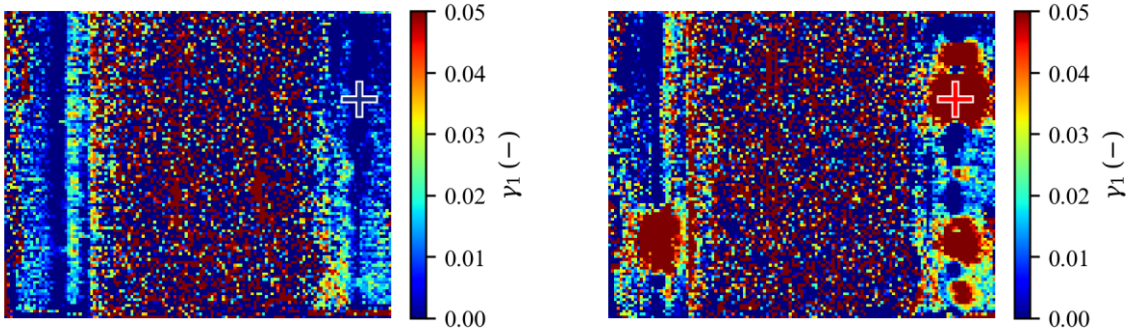

(a) (b)

Figure 6: Image post-processing example on a damaged sample under cyclic bending at $R_{nom} = 10$ - Field of the skewness γ_1 at $N = 5\,000$ cycles (a) and at $N = 210\,000$ cycles showing presence of one crack on the left weld toe and five on the right weld toe (b) – The temperature signals θ^c_{the} at the coloured cross markers are illustrated in Figure 5 a

2.3.4 Occurrence of the closing phenomenon

A clear distinction of the crack propagation phenomena exists between both loading cases ($R_{nom} = 0.1$ and $R_{nom} = 10$). To properly detect cracks, the relevant post-processing operation must be chosen: either the evaluation of the temperature's first harmonic θ_1^c via the lock-in method [31] (for open cracks) or the evaluation of the skewness γ_1 of the temperature signal (for closing cracks). Indeed, for open cracks, the skewness indicator γ_1 is ineffective (Figure 4 c); on the contrary, for closing cracks, the first harmonic indicator θ_1^c is not suitable (Figure 6 b). In this study, it was verified (by estimating γ_1) that no closing phenomenon exists at $R_{nom} = 0.1$; on the contrary, it was also verified that such closing phenomenon always exists at $R_{nom} = 10$. As a result, there is no ambiguity as to which method must be applied for each testing configuration.

3 Experimental results

In this section, experimental results (namely the fatigue lives and the collected infrared data) are detailed and discussed.

3.1 Fatigue results

In order to assess the fatigue properties of the T-joints, the choice of an adequate criterion for the definition of a fatigue life must be made. Indeed, fatigue failure is reached for specimens tested at $R_{nom} = 0.1$ (critical crack depth leading to sensible drop in the T-joint stiffness), but it is not for specimens tested at $R_{nom} = 10$ for which the in-depth propagation of cracks seems to either stop or evolve very slowly. In that regard, joint AS-W-R10-1 constitutes a pathological case, for which fatigue failure was observed not at the weld toe, but on the opposite face, in the bulk. For this reason, two fatigue lives are considered in this study:

- the number of cycles to TSA crack detection N_d;
- the number of cycles to weld long crack N_t, *i.e.* when a unique crack of length l_T is observed at the weld toe on infrared data.

The fatigue lives of the tested T-joints are given in Table 2.

Sample	$\frac{\Delta\sigma_{nom}}{\sigma_y}$ $(-)$	N_d $(cycles)$	N_t $(cycles)$	$\frac{da}{dN}$ $(mm/cycle)$
AS-W-R01-1	0.29	134 000	320 000	3.7×10^{-5}
AS-W-R01-2	0.66	4 200	21 000	3.6×10^{-4}
AS-W-R01-3	0.86	4 000	16 500	5.0×10^{-4}
PRE-T-R01-1	0.66	7 000	23 500	3.0×10^{-4}
AS-W-R10-1	0.66	90 000	$> 288\,000$	1.9×10^{-5}
AS-W-R10-2	1.13	3 000	12 000	2.6×10^{-4}
PRE-C-R10-1	0.66	80 000	330 000	3.0×10^{-5}
PRE-C-R10-2	0.86	36 000	160 000	1.1×10^{-4}
PRE-C-R10-3	1.13	4 000	15 000	3.1×10^{-4}

Table 2: Number of cycles to crack detection N_d, number of cycles to weld long crack N_t and crack growth rate $\frac{da}{dn}$ (for $a \in [1:5]$) for all tested T-joints (a > sign means the test was stopped before a crack reached the total length of the weld toe)

In Figure 7, the normalised stress range $\frac{\Delta\sigma_{nom}}{\sigma_y}$ is plotted against the fatigue life N_t in a log-log diagram. The data points of specimens tested at $R_{nom} = 0.1$ seem to be aligned in a straight line, following a Basquin law

$$N_t = C_B \Delta\sigma_{nom}{}^{-m_B}, \quad (8)$$

of slope $m_B = 2.8$. This can be justified by the fact that these specimens have very close effective stress ratios R_{eff} (Table 1). On the contrary, T-joints tested at $R_{nom} = 10$ do not show such linear trend, which is again coherent with the fact that their respective effective stress ratios R_{eff} are different (Table 1).

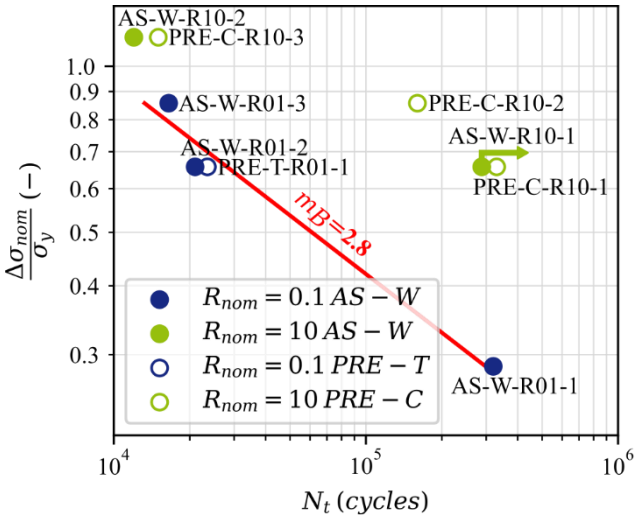

Figure 7: Number of cycles to weld long crack N_d of all tested T-joints and Basquin trend of $R_{nom} = 0.1$ specimens

3.2 Infrared data post-processing

Given the experimental protocol as presented in previous paragraph, the collected infrared data and its post-processing allows for the monitoring of fatigue cracks at the weld toes. From this monitoring the propagation kinetics of the fatigue cracks is characterized and linked to the fatigue properties of the T-joints.

In the following figures, the number of cycles is normalized with respect to the total number of cycles N_r at the end of the test.

3.2.1 Propagation maps

For each film that is recorded during the fatigue test, the adapted crack indicator map is computed (the temperature's first harmonic differential $\Delta\theta_1^c$ at $R_{nom} = 0.1$ or the skewness γ_1 at $R_{nom} = 10$). On these maps, two rectangular regions of interest are defined, bounding each weld toe (left and right). The crack indicator field in these regions is averaged along the weld toe's width only to retain the information of the position and length of cracks along the weld toe's length. The evolution of the position and length of the cracks during the fatigue test is then compiled in a propagation map. This whole process is illustrated on the case of the sample AS-W-R01-1 left weld toe in Figure 8. The propagation maps of four different weld toes for different samples are plotted in Figure 9.

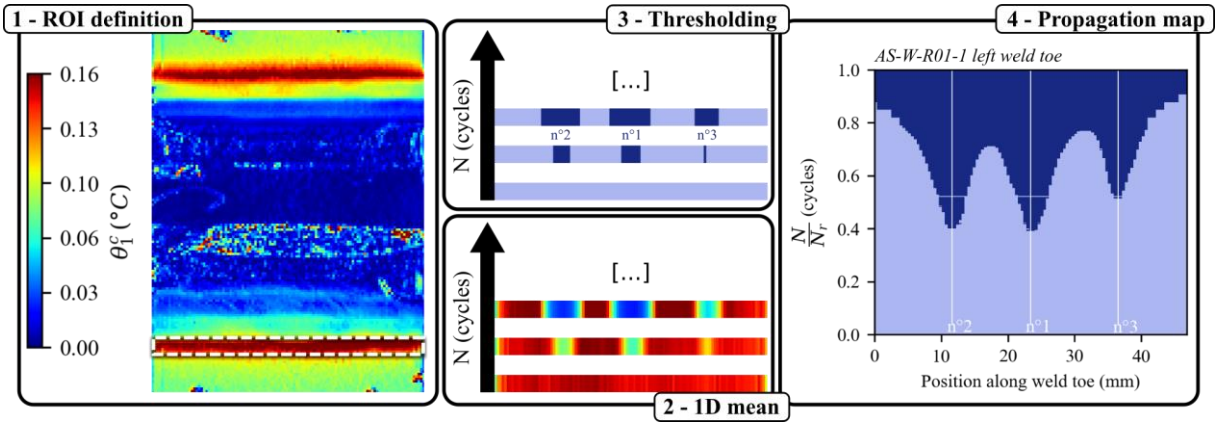

Figure 8: Schematic illustration of the propagation map construction: firstly a Region Of Interest (ROI) is defined to delimit one weld toe in the crack indicator map, secondly the 1D mean of the ROI along the weld toe thickness is computed for each time increment *N*, thirdly the thresholding of each 1D mean is computed to retain only the information of the position and length of a crack along the weld toe, finally the binarized 1D images are stacked to create the propagation map

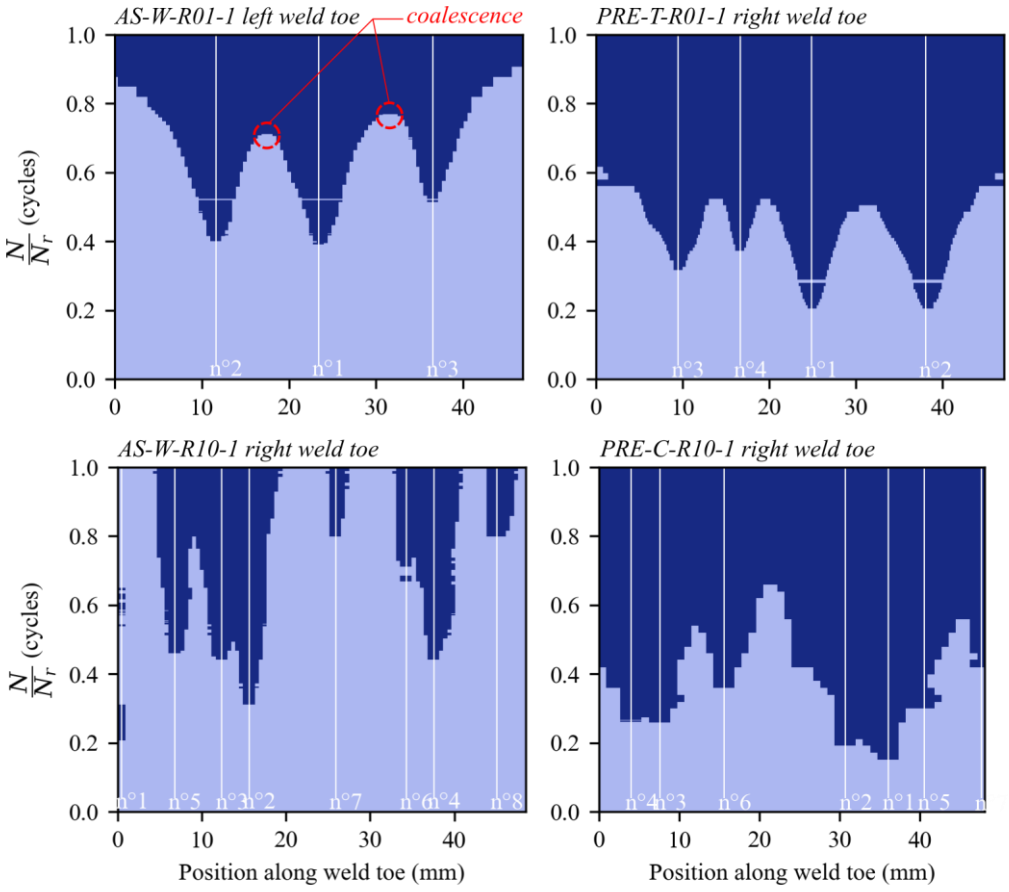

Figure 9: Example of crack propagation maps for samples AS-W-R01-1, PRE-T-R01-1, AS-W-R10-1 and PRE-C-R10-1

The initiation of multiple cracks at the weld toe is systematic. As a result, cracks can undergo a coalescence phenomenon (merging of cracks, Figure 9). The merging of cracks leads to the formation of a unique crack that eventually extends over the whole length of the weld toe at the number of cycles N_t. The lifetime N_t estimated for each sample is given in Table 2.

The number of cycles corresponding to the first infrared film for which a crack is detected is denoted by N_d. It is then possible to estimate a propagation life ratio $r_p^d = \frac{N_t - N_d}{N_t}$. In this study, it was determined for all tested sample that this ratio is on average equal to 73% (Figure 10), meaning that most of the fatigue life of the T-joints consists in fatigue crack propagation. It is believed, due to image resolution and conduction effects, that the number of cycles to first crack detection N_d is larger than the number of cycles N_i for actual crack initiation. As a result, the detected propagation life ratio r_p^d is smaller than the real propagation life ratio $r_p^i = \frac{N_t - N_i}{N_t}$. From this result, it appears the crack initiation phase is negligible; a crack propagation approach is well suited to the description of the fatigue life of T-joints.

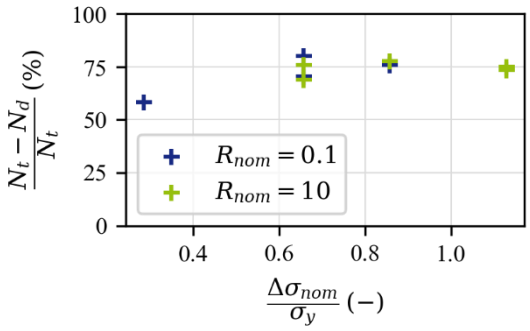

Figure 10: Propagation life ratio of the tested T-joints

3.2.2 Propagation curves

In order to characterize the propagation kinetics at the different loading conditions, the detected fatigue cracks are distinguished and their length $2a$ along the weld toe is plotted against the number of cycles N (Figure 11). These propagation curves show linear evolution for large non-coalescent cracks (for $2a$ from about $2mm$ up to $10mm$) of identical slope. Then, the propagation speed $\frac{\mathrm{d}a}{\mathrm{d}N}$ of given loading configuration is assimilated to the mean slope of the crack propagation curves in their linear domain. The estimated propagation speed $\frac{\mathrm{d}a}{\mathrm{d}N}$ of the tested T-joints is detailed in Table 2.

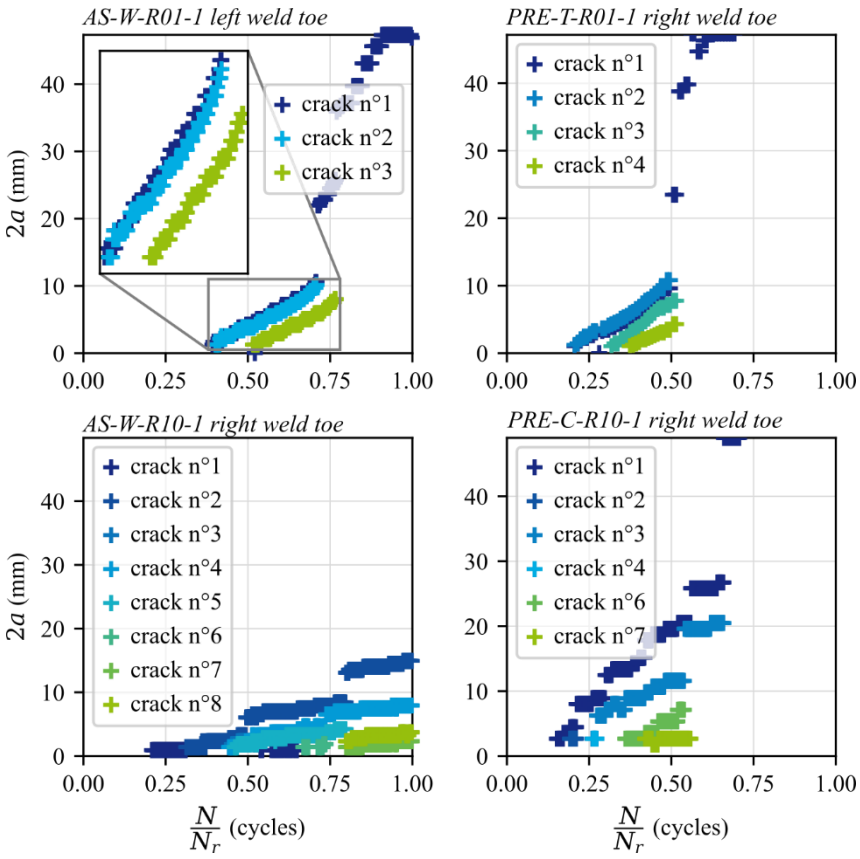

Figure 11: Example of crack propagation curves for samples AS-W-R01-1, PRE-T-R01-1, AS-W-R10-1 and PRE-C-R10-1

Comparing the propagation speed $\frac{\mathrm{d}a}{\mathrm{d}N}$ of samples AS-W-R10-1 and AS-W-R10-2 to that of AS-W-R01-1, AS-W-R01-2 and AS-W-R01-3, it can be noticed that cracks propagate considerably slower for $R_{nom} = 10$ than for $R_{nom} = 0.1$ when considering a same initial state (as-welded). This is caused by the crack closing phenomenon that exists for $R_{nom} = 10$. As a result, the number of cycles N_t needed to reach the maximum crack length of as-welded T-joints is greater for $R_{nom} = 10$ than for $R_{nom} = 0.1$. It can be verified that, when comparing two loading configurations, a smaller propagation speed $\frac{\mathrm{d}a}{\mathrm{d}N}$ leads to a greater life span N_t (Table 2).

4 A model considering the effective stress ratio effect

The proposed model is based on a fatigue crack propagation approach in which the closing phenomenon related to the effective stress ratio R_{eff} is considered. First, the different ingredients of the model are detailed, then the model identification process is exposed and finally the model is validated by confrontation to experimental fatigue data.

4.1 Model philosophy

The proposed approach neglects the initiation phase and assumes the existence of initial cracks at the weld toe which propagation in fatigue is described by the Paris-Erdogan law [14]

$$\frac{\mathrm{d}a}{\mathrm{d}N} = C_p \Delta K^{m_p}, \qquad 9$$

with C_p and m_p material parameters of the law and ΔK the stress intensity factor's range. The range ΔK is defined as

$$\Delta K = F(a)\Delta\sigma_{eff}\sqrt{\pi a}, \quad 10$$

where $F(a)$ is a correction factor and $\Delta\sigma_{eff}$ the effective stress range. The factor $F(a)$ is used for the consideration of multiple effects depending on the studied configuration such as edge effects (finite width and thickness), the type of loading (tension, bending, *etc*) as well as the size and shape of the crack front. The effective stress range $\Delta\sigma_{eff}$ is determined as the stress range that effectively participates in the propagation of the fatigue crack. In that context, r_o represents the share of the nominal stress range that contributes to the crack propagation. The paramater r_o is itself dependent on the effective stress ratio R_{eff}

$$\Delta\sigma_{eff} = r_o(R_{eff})\Delta\sigma_{nom}. \quad 11$$

Finally, combining equations 9 to 11, it is possible to determine the number of cycles corresponding to the propagation of a non-coalescent crack of an initial half-length a_0 to a half-length a_f

$$N(a = a_f) = \frac{1}{C_p\left[r_o(R_{eff})\Delta\sigma_{nom}\right]^{m_p}} \int_{a_0}^{a_f} \frac{1}{\left(F(a)\sqrt{\pi a}\right)^{m_p}} \mathrm{d}a. \quad 12$$

In order to use such model, the parameters C_p, m_p and a_0 are determined from the infrared data, as well as parameter $r_o(R_{eff})$. The correction factor $F(a)$ is determined from the literature, to best match the configuration of the fatigue cracks at the weld toe of bending T-joints.

4.2 Model identification

4.2.1 Stress intensity factor

The stress intensity factor's range ΔK is completely determined by the definition of the correction factor $F(a)$ (equation 10). In the particular case of fatigue cracks at the weld toe of T-joints, the correction factor as defined by Recho [34] is adopted, in which it is proposed to combine two correction factors from the literature, namely $Y(a)$ for surface cracks in a finite three-dimensional body, as defined by Newman and Raju [35], and $M_k(a)$ for welded T-joints, as defined by Hobbacher [36], following

$$F(a) = Y(a)M_k(a). \quad 13$$

The first term $Y(a)$ is defined as

$$Y(a) = \frac{f_w}{\sqrt{Q}}\left[M_1 + M_2\left(\frac{c}{e}\right)^2 + M_3\left(\frac{c}{e}\right)^4\right], \quad 14$$

where c is the crack depth, f_w a parameter relative to the finite width of the joint, Q a parameter relative to the crack front shape and M_1, M_2 and M_3 parameters dependent of the considered position at the crack front (in the present case $F(a)$ is expressed at the bottom of the crack front). These parameters are defined by the following expressions

$$\begin{cases} f_w = \sqrt{\sec\left[\frac{\pi}{l_T/e_T}\frac{1}{c/a}\sqrt{\left(\frac{c}{e_T}\right)^3}\right]}; \\ Q = 1 + 1.464\left(\frac{c}{a}\right)^{1,65}; \\ M_1 = 1.13 - 0.09\frac{c}{a}; \\ M_2 = \frac{0.89}{0.2 + \frac{c}{a}} - 0.54; \\ M_3 = 0.5 - \frac{1}{0.65 + \frac{c}{a}} + 14\left(1 - \frac{c}{a}\right)^{24}; \end{cases} \quad 15$$

with l_T the joint's width and e_T the joint's thickness (Figure 1).

The second term $M_k(a)$ is defined as

$$M_k(a) = v\left(\frac{c}{e_T}\right)^w, \quad 16$$

with

$$\begin{cases} v = 0.8068 - 0.1554\frac{H_w}{e_T} + 0.0429\left(\frac{H_w}{e_T}\right)^2 + 0.0794\frac{W_w}{e_T}; \\ w = -0.1993 - 0.1839\frac{H_w}{e_T} + 0.0495\left(\frac{H_w}{e_T}\right)^2 + 0.0815\frac{W_w}{e_T}; \end{cases} \quad 17$$

where W_w is the weld width and H_w is the weld height (Figure 1). It must be noted that in this study the T-joints are built so that $H_w = W_w$.

In practice, the infrared thermography experimental protocol presented in the previous paragraphs only allows for the monitoring of the crack surface length $2a$ while the depth c remains unknown. In the present case, we chose to adopt the empiric law defined by Carteron *et al.* [8] in a very similar configuration (high-strength steel cruciform welded-joints loaded in tension), formulated as such

$$c(a) = -0.48a^{1.14} + a. \quad 18$$

This hypothesis appears acceptable when confronted to the fractography analysis of a failed T-joint (Figure 12).

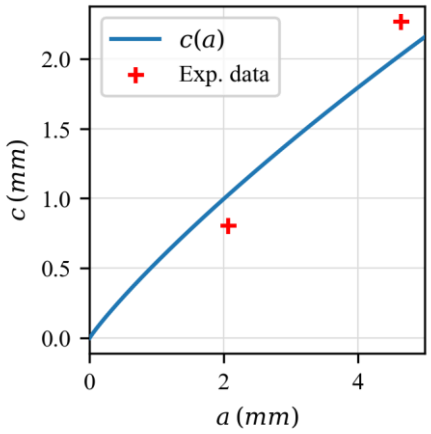

Figure 12: Evolution of the depth c as a function of the surface half-length a as proposed by Carteron *et al.* [8]

4.2.2 Paris-Erdogan law's exponent m_p

As shown in paragraph 3.2, the crack half-length a is linear with respect to the number of cycles N for millimetric cracks (between approximately 2 and 10 millimeters). In that regard, the crack growth rate $\frac{\mathrm{d}a}{\mathrm{d}N}$ of millimetric cracks is independent of the crack half-length a ($\frac{\mathrm{d}^2a}{\mathrm{d}N\mathrm{d}a} = 0$ for $a \in [2:10]$). Given the Paris-Erdogan law (eq. 9), the form of the stress intensity range ΔK (eq. 10) and the expression of the effective stress range $\Delta\sigma_{eff}$ (eq. 11), for millimetric cracks, it comes

$$\frac{\mathrm{d}a}{\mathrm{d}N} \propto \left[r_o\left(R_{eff}\right)\right]^{m_p} \Delta\sigma_{nom}^{m_p}. \qquad 19$$

Then, the slope of the evolution of the crack growth rate of millimetric cracks $\frac{\mathrm{d}a}{\mathrm{d}N}$ with respect to the applied nominal stress range $\Delta\sigma_{nom}$ in logarithmic scale, for a constant effective stress ratio R_{eff}, is equal to the Paris-Erdogan exponent m_p. The values of $\frac{\mathrm{d}a}{dN}$ (Table 2) are plotted against $\Delta\sigma_{nom}$ in a log-log diagram for all tested T-joints in Figure 13. The Paris-Erdogan exponent m_p is identified as the slope formed by data points of specimens AS-W-R01-1, AS-W-R01-2 and AS-W-R01-3, which effective stress R_{eff} is very close to 0.1. Moreover, crack closure was not witnessed through TSA for these specimens. The value of the Paris-Erdogan exponent is then $m_p = 2.4$.

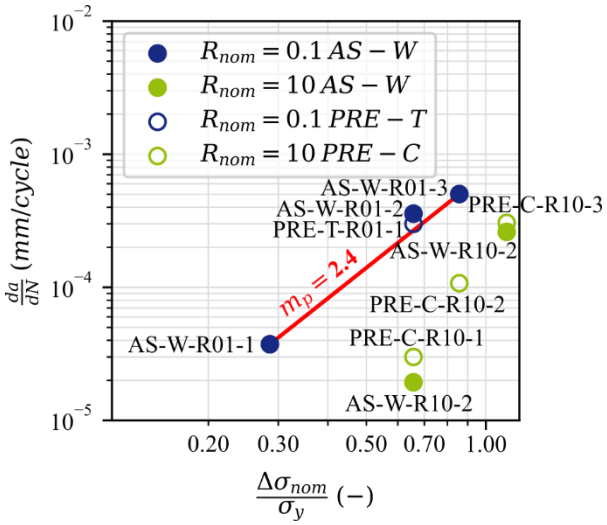

Figure 13: Identification of the Paris-Erdogan exponent m_p as the slope of the evolution of $\frac{\mathrm{d}a}{\mathrm{d}N}$ with respect to $\Delta\sigma_{nom}$ in a logarithmic scale for millimetric cracks at a constant effective stress ratio R_{eff}

4.2.3 Effective stress range

The analysis of infrared films of T-joints under cyclic bending revealed the existence of a fatigue crack closing phenomenon at $R_{nom} = 10$ (paragraph 2.3). For such configurations, only a portion of the nominal stress range $\Delta\sigma_{nom}$ effectively takes part in the propagation of the initiated fatigue cracks: the effective stress range $\Delta\sigma_{eff}$. This effective stress range depends on the opening rate of the fatigue crack within one loading cycle r_o, for which the following definition is proposed

$$\Delta\sigma_{eff} = r_o\left(R_{eff}\right)\Delta\sigma_{nom} = \frac{1 - b^* R_{eff}}{1 - R_{eff}}\Delta\sigma_{nom};$$
$$with\ b^* = \begin{cases} 1\ si\ 1 > R_{eff} \geq 0 \\ b\ otherwise \end{cases}; \qquad 20$$

where b is a material parameter. From this definition of the opening rate r_o, and from equation 19, it is determined that for millimetric cracks, $\log\left(\frac{\mathrm{d}a}{\mathrm{d}N}\right)$ is linear with respect to $\log\left(\Delta\sigma_{eff}\right)$ with a slope of m_p.

Then, the parameter b can be estimated by a linear least-square best fit on experimental data (Table 2). The value $b = 0.43$ is found, for which all data points are aligned in a $\left(\frac{da}{dN}; \Delta\sigma_{eff}\right)$ diagram in log-log scale (Figure 14). While the crack growth rates $\frac{da}{dN}$ seem to form two distinct datasets when plotted against the nominal stress range $\Delta\sigma_{nom}$ (Figure 13), the definition of an effective stress range $\Delta\sigma_{eff}$ demonstrates the existence of a global linear tendency in log-log scale (Figure 14).

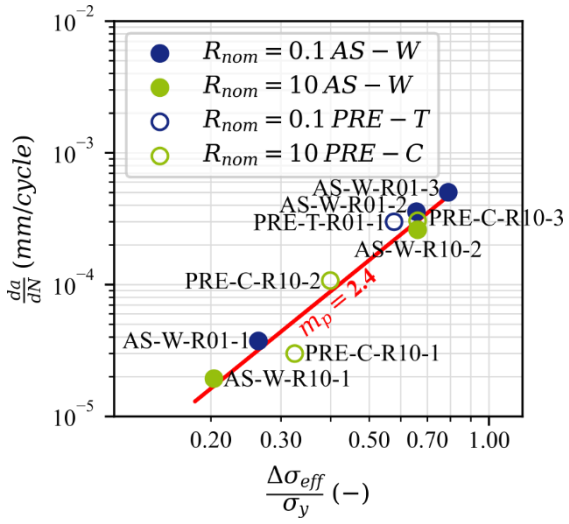

Figure 14: Alignment of the experimental data points in the $\left(\frac{da}{dN}; \Delta\sigma_{eff}\right)$ in log-log scale by the least-squares method to estimate the parameter b

From the expression of the effective stress range $\Delta\sigma_{eff}$, and considering the loadings with $R_{eff} = -1$ and $R_{eff} = 0$, it comes

$$\frac{1+b}{2}\Delta\sigma_{nom,R_{eff}=-1} = \Delta\sigma_{nom,R_{eff}=0} \qquad 21$$

or

$$\frac{1}{2}\Delta\sigma_{nom,R_{eff}=-1} = \frac{1}{2}\Delta\sigma_{nom,R_{eff}=0}\left(1+\frac{1-b}{1+b}\right). \qquad 22$$

Equation 22 can be rewritten

$$\frac{1}{2}\Delta\sigma_{nom,R_{eff}=0} = \frac{1}{2}\Delta\sigma_{nom,R_{eff}=-1} - m_R\sigma_{m|R_{eff}=0}, \qquad 23$$

where the parameter m_R depends on b following

$$m_R = \frac{1-b}{1+b}, \qquad 24$$

and where $\sigma_{m|R_{eff}=0} = \frac{\sigma_{min}+\sigma_{max}}{2} + \sigma_{res}$ is the mean stress at $R_{eff} = 0$. In the same manner, for any effective stress ratio R^*_{eff}

$$\frac{1}{2}\Delta\sigma_{nom,R_{eff}=R^*_{eff}} = \frac{1}{2}\Delta\sigma_{nom,R_{eff}=-1} - m^*_R\,\sigma_{m|R_{eff}=R^*_{eff}},$$
$$m^*_R = \begin{cases} m_R\left(\frac{1-R^*_{eff}}{1+R^*_{eff}}\right)\ if\ 1 > R^*_{eff} \geq 0 \\ m_R\ otherwise \end{cases}. \qquad 25$$

The parameter m_R describes the material sensitivity to the effective stress ratio R_{eff} in fatigue. According to the expression of m^*_R (eq. 25), the fatigue failure curve in the Haigh diagram for a fixed

number of cycles N is bilinear, with a slope of $-m_R$ for effective stress ratios R_{eff} under 0 and above 1 and a zero slope otherwise (Figure 15). Such behaviour is comparable to experimental observations as described in the work of Hensel [13].

Considering the value $b = 0.43$, the corresponding stress ratio sensitivity parameter m_R is equal to 0.39, which is again coherent with experimental results from the work of Hensel [13], where values of m_R between 0.2 and 0.4 for longitudinal welded stiffeners are given.

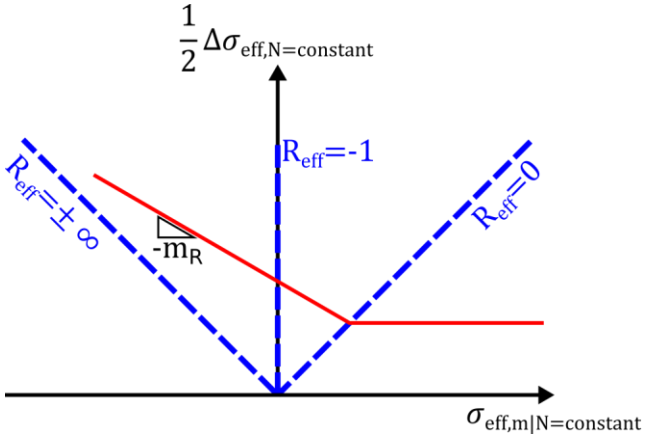

Figure 15: Fatigue failure curve in the Haigh diagram for a constant number of cycles *N* as per the proposed model

4.2.4 Best-fit of the crack propagation law

Two parameters of the proposed model are still to be determined: the initial crack size a_0 and the Paris-Erdogan coefficient C_p. They are both determined through a single operation of minimization of the least square error of the propagation law (eq. 12) as compared to experimental data of non-coalescent millimetric cracks propagation. In this study, portions of the cracks n°1 and n°2 of specimen AS-W-R01-1 (half-length a between 1 and 5 mm, Figure 11) were chosen as the optimization database (as it is a case without crack closure). Values $a_0 = 0.04\ mm$ and $C_p = 3{,}5 \times 10^{-14}\ mm^{1-\frac{m_p}{2}}.MPa^{-m_p}$ are then estimated.

4.2.5 Model identification results

Finally, the fatigue model based on a crack propagation approach is fully identified on the basis of the infrared thermography monitoring of T-joints under cyclic bending. The values of the model's parameters are summarized in Table 3.

m_p (−)	C_p $(mm^{1-\frac{m_p}{2}}.MPa^{-m_p})$	b (−)	a_0 (mm)
2,4	$3{,}5 \times 10^{-14}$	0,43	0,04

Table 3: Identified values of the parameters of the crack propagation model

4.3 Model validation

4.3.1 Choice of a stop criterion a_f

The proposed fatigue model (eq. 12) is based on a crack propagation approach: the existence of an initial crack is assumed, and the model describes its propagation according to the number of cycles N. The fatigue life estimated using this method is necessarily associated to the choice of a final crack length a_f. This crack length a_f is a useful parameter to adjust the degree of conservatism of the fatigue life forecast.

In the present configuration, care must be taken to consider a crack length a for which the coalescence phenomenon is unlikely to happen as the model is not fit to describe the propagation of coalesced cracks which shape and evolution is more complex to predict. The infrared thermography monitoring has shown that multiple cracks initiate systematically for all specimens. As a result, a coalescence phenomenon is also systematically observed. According to the propagation curves determined from infrared data (Figure 11), cracks usually propagate up to a full-length $2a$ of 10 mm before coalescence. In that context, the value a_f must be chosen under 5 mm to describe the life of the T-joints.

In the following paragraph, a_f is chosen equal to 5 mm in order to compare the fatigue forecasts of the model to the experimental fatigue lives N_t (number of cycles to formation of a full-width crack on the T-joint). Indeed, as soon as the coalescence phenomenon arises, the propagation of cracks significantly accelerates until a full-width crack is formed. As a result, the number of cycles difference between the instant of first crack coalescence $N_c \approx N(a_f = 5)$ and the instant N_t is small in comparison to N_t. In this context, while the choice of $a_f = 5\,mm$ is inherently conservative as $N(a_f) \leq N_t$, the direct comparison of $N(a_f)$ to N_t as validation of the approach taking into account the stress ratio effect is justified.

4.3.2 Confrontation to experimental fatigue life N_t

The fatigue life forecasts according to the proposed model, for $a_f = 5\,mm$ and with parameters identified from infrared data, are compared to the experimental fatigue life N_t, corresponding to the number of cycles when a crack is spread over the entire width of the T-joint, on either the left or right weld toe. Results are plotted in Figure 16, with the experimental values N_t on the x-axis and the model forecast $N(a_f = 5)$ on the y-axis. The black solid line represents the ideal prediction where $N(a_f = 5) = N_t$ and the two dotted lines represent a prediction error of plus or minus one decade.

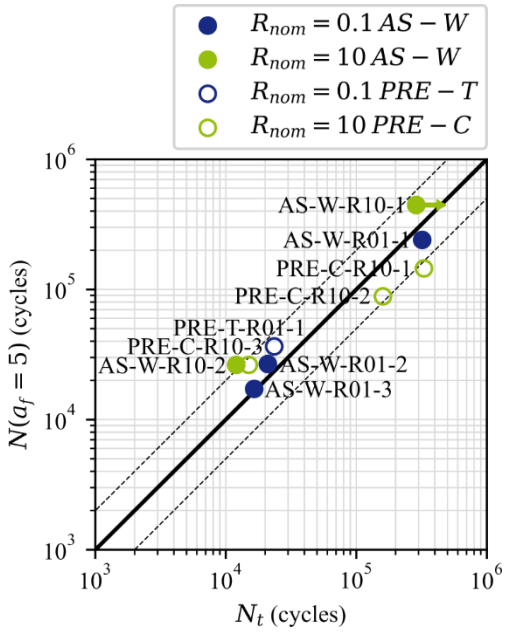

Figure 16: Comparison of the fatigue forecast $N(a_f = 5)$ to the experimental fatigue life N_t with consideration of the stress ratio effect ($b = 0.43$)

The model predictions are satisfactory as most lie within two decades of the experimental lifetime N_t. The most conservative forecast is made for specimen PRE-C-R10-1 (as it could be expected from its crack growth rate, Figure 14). It is important to note that the experimental fatigue lives N_t are not involved in the assessment of the model's parameters.

5 Conclusion

The effect of residual stresses and stress ratio on the high-cycle fatigue behaviour of high-strength steel welded T-joints was investigated in this study. On the basis of the experimental results, the following observations were made:

1. Important transversal residual stresses exist at the weld toe in the as-welded condition. This initial field is only affected by large amplitude cyclic loadings ($\frac{\Delta\sigma_{nom}}{\sigma_y} > 0.66$).
2. The TSA protocol adopted allows for millimetric crack monitoring at the weld toe. Moreover, it allows for the indirect observation of the crack closure phenomenon because of the non-linear thermoelastic response in the vicinity of the crack.
3. The fatigue life of the as-welded joints is dominated by a crack propagation phase.

Through the proposition of a LEFM based model and its identification based on TSA observations, the following conclusions can be drawn:

1. The Paris-Erdogan law can be fully determined on the basis of the TSA crack monitoring results, with the exception of the relation between surface and in-depth propagation that requires test interruptions.
2. An effective stress range $\Delta\sigma_{eff}$ was defined, which is chosen dependent on the effective stress ratio R_{eff} according to the parameter b^* which value is determined by the unification of fatigue crack growth rates for different load ratios.
3. The parameter b^* allows for the calculation of the mean stress sensitivity factor ${m_R}^*$ which value is coherent with literature data, as found in the work by Hensel [13].
4. The fatigue forecasts are in good agreement with experimental fatigue lives N_t, validating the model in the studied configuration of high-strength steel welded T-joints. Such forecasts require the prior knowledge of residual stresses at the weld toe.

Acknowledgements

The authors would like to thank Direction Générale de l'Armement (DGA) for its support. This work was completed as part of the Gustave Zédé joint-lab collaborative research between Naval Group and ENSTA Bretagne.

References

1 Williams HE, Ottsen H, Lawrence F V, Munse WH. The Effects of Weld Geometry on the Fatigue Behavior of Welded Connections. *Illinois Coop Highw Res Progr*. 1970.

2 Alam MM, Barsoum Z, Jonsén P, Häggblad HA, Kaplan AFH. Geometrical aspects of the fatigue behaviour of laser hybrid fillet welds. *Proc Fatigue Des Conf*. 2009.

3 Barsoum Z, Barsoum I. Residual stress effects on fatigue life of welded structures using LEFM. *Eng Fail Anal*. 2009;16: 449–467.

4 Sonsino CM. Effect of residual stresses on the fatigue behaviour of welded joints depending on loading conditions and weld geometry. *Int J Fatigue*. 2009;31: 88–101.

5 Martins Ferreira JA, Moura Branco CA. Influence of the radius of curvature at the weld toe in the fatigue strength of fillet welded joints. *Int J Fatigue*. 1989;11: 29–36.

6 Chaudhuri S, Crump J, Reed PAS, Mellor BG. High-resolution 3D weld toe stress analysis and ACPD method for weld toe fatigue crack initiation. *Weld World*. 2019;63: 1787–1800.

7 Kirkhope KJ, Bell R, Caron L, Basu RI, Ma KT. Weld detail fatigue life improvement

techniques. Part 1: Review. *Mar Struct*. 1999;12: 447–474.

8 Carteron L, Doudard C, Calloch S, Levieil B, Beaudet J, Bridier F. Naval welded joints local stress assessment and fatigue cracks monitoring with quantitative thermoelastic stress analysis. *Theor Appl Fract Mech*. 2020;110: 102792.

9 Murugan S, Rai SK, Kumar P V., Jayakumar T, Raj B, Bose MSC. Temperature distribution and residual stresses due to multipass welding in type 304 stainless steel and low carbon steel weld pads. *Int J Press Vessel Pip*. 2001;78: 307–317.

10 Leggatt RH. Residual stresses in welded structures. *Int J Press Vessel Pip*. 2008;85: 144–151.

11 Turski M, Francis JA, Hurrell PR, Bate SK, Hiller S, Withers PJ. Effects of stop-start features on residual stresses in a multipass austenitic stainless steel weld. *Int J Press Vessel Pip*. 2012;89: 9–18.

12 Farajian M, Nitschke-Pagel T, Dilger K. Mechanisms of residual stress relaxation and redistribution in Welded high-strength steel specimens under mechanical loading. *Weld World*. 2010;54: 366–374.

13 Hensel J. Mean stress correction in fatigue design under consideration of welding residual stress. *Weld World*. 2020: 535–544.

14 Paris P, Erdogan F. A critical analysis of crack propagation laws. *J Fluids Eng Trans ASME*. 1963;85: 528–533.

15 Forman RG, Kearney VE, Engle RM. Numerical analysis of crack propagation in cyclic-loaded structures. *J Fluids Eng Trans ASME*. 1967;89: 459–463.

16 Walker K. The Effect of Stress Ratio During Crack Propagation and Fatigue for 2024-T3 and 7075-T6 Aluminum. In: *Effects of Environment and Complex Load History on Fatigue Life*. 100 Barr Harbor Drive, PO Box C700, West Conshohocken, PA 19428-2959: ASTM International; 1970:1-1–14.

17 Mettu SR, Shivakumar V, Beek JM, *et al*. NASGRO 3.0 - A Software For Analyzing Aging Aircraft. In: *The Second Joint NASA/FAA/DoD Conference on Aging Aircraft*. ; 1999.

18 Smith IFC, Smith RA. Fatigue crack growth in a fillet welded joint. *Eng Fract Mech*. 1983;18: 861–869.

19 Sakagami T, Mizokami Y, Shiozawa D, Izumi Y, Moriyama A. TSA based evaluation of fatigue crack propagation in steel bridge members. *Procedia Struct Integr*. 2017;5: 1370–1376.

20 De Finis R, Palumbo D, Carolo F Di, Ricotta M, Meneghetti G, Galietti U. Crack tip position evaluation and Paris' law assessment of a propagating crack by means of temperature-based approaches. *Procedia Struct Integr*. 2021;39: 528–545.

21 Ummenhofer T, Medgenberg J. On the use of infrared thermography for the analysis of fatigue damage processes in welded joints. *Int J Fatigue*. 2009;31: 130–137.

22 Fan J, Zhao Y. Quantitative thermography for fatigue damage assessment and life prediction of welded components. *Mech Mater*. 2022;164: 104120.

23 Florin P, Facchinetti M, Doudard C, Calloch S. Fast fatigue properties identification by "self-heating" method: Application to automotive welded joints. *Procedia Eng*. 2013;66: 676–683.

24 Zhang HX, Wu GH, Yan ZF, Guo SF, Chen PD, Wang WX. An experimental analysis of fatigue behavior of AZ31B magnesium alloy welded joint based on infrared thermography. *Mater Des*. 2014;55: 785–791.

25 Crupi V, Guglielmino E, Maestro M, Marinò A. Fatigue analysis of butt welded AH36 steel

joints: Thermographic Method and design S-N curve. *Mar Struct*. 2009;22: 373–386.

26 Palumbo D, Galietti U. Characterisation of steel welded joints by infrared thermographic methods. *Quant Infrared Thermogr J*. 2014;11: 29–42.

27 La Rosa G, Risitano A. Thermographic methodology for rapid determination of the fatigue limit of materials and mechanical components. *Int J Fatigue*. 2000;22: 65–73.

28 Williams P, Liakat M, Khonsari MM, Kabir OM. A thermographic method for remaining fatigue life prediction of welded joints. *Mater Des*. 2013;51: 916–923.

29 Amiri M, Khonsari MM. Nondestructive estimation of remaining fatigue life: Thermography technique. *J Fail Anal Prev*. 2012;12: 683–688.

30 Boulanger T, Chrysochoos A, Mabru C, Galtier A. Calorimetric analysis of dissipative and thermoelastic effects associated with the fatigue behavior of steels. *Int J Fatigue*. 2004;26: 221–229.

31 Breitenstein O, Warta W, Langenkamp M. *Lock-in Thermography - Basics and Use for Evaluating Electronic Devices and Materials*. Berlin: Springer; 2010.

32 Brémond P, Potet P. Lock-In Thermography : A tool to analyse and locate thermo-mechanical mechanisms in materials and structures. In: *Proceedings SPIE 4360, Thermosens XXII*. Vol 4360. ; 2001:560–566.

33 Sakagami T. Remote nondestructive evaluation technique using infrared thermography for fatigue cracks in steel bridges. *Fatigue Fract Eng Mater Struct*. 2015;38: 755–779.

34 Recho N. *Mécanique de Propagation et Bifurcation Des Fissures*. (Lavoisier C: HS:, ed.).2012.

35 Newman JC, Raju IS. Stress Intensity Factor Equations for Cracks in Three-Dimensional Bodies Subjected to Tension and Bending Loads. *NASA Tech Memo*. 1984.

36 Hobbacher A. Stress intensity factors of welded joints. *Eng Fract Mech*. 1993;46: 173–182.